Structure and Mechanism of Chitin Deacetylase from the Fungal Pathogen *Colletotrichum lindemuthianum*[†,‡]

David E. Blair,[§] Omid Hekmat,[||] Alexander W. Schüttelkopf,[§] Binesh Shrestha,[⊥] Ken Tokuyasu,[#] Stephen G. Withers,[||] and Daan M. F. van Aalten*[,§]

Division of Biological Chemistry and Molecular Microbiology, School of Life Sciences, University of Dundee, Dundee DD1 5EH, Scotland, Protein Engineering Network of Centres of Excellence of Canada, Department of Chemistry, University of British Columbia, 2036 Main Mall, Vancouver, British Columbia, Canada V6T 1Z1, Institut de Génétique et Microbiologie, Université Paris-Sud, Bât 360, Orsay 91405, France, and Carbohydrate Laboratory, Food Material Division, National Food Research Institute, 2-1-12 Kannondai, Tsukuba, Ibaraki 305-8642, Japan

Received April 5, 2006; Revised Manuscript Received June 6, 2006

ABSTRACT: The fungal pathogen *Colletotrichum lindemuthianum* secretes an endo-chitin de-*N*-acetylase (*Cl*CDA) to modify exposed hyphal chitin during penetration and infection of plants. Although a significant amount of biochemical data is available on fungal chitin de-*N*-acetylases, no structural data exist. Here we describe the 1.8 Å crystal structure of a *Cl*CDA product complex and the analysis of the reaction mechanism using Hammett linear free energy relationships, subsite probing, and atomic absorption spectroscopy studies. The structural data in combination with biochemical data reveal that *Cl*CDA consists of a single domain encompassing a mononuclear metalloenzyme which employs a conserved His-His-Asp zinc-binding triad closely associated with the conserved catalytic base (aspartic acid) and acid (histidine) to carry out acid/base catalysis. The data presented here indicate that *Cl*CDA possesses a highly conserved substrate-binding groove, with subtle alterations that influence substrate specificity and subsite affinity. Strikingly, the structure also shows that the hexahistidine purification tag appears to form a tight interaction with the active site groove. The enzyme requires occupancy of at least the 0 and +1 subsites by $(GlcNAc)_2$ for activity and proceeds through a tetrahedral oxyanion intermediate.

Colletotrichum lindemuthianum is a plant fungal pathogen found extensively in tropical and subtropical regions. *Colletotrichum* species are the causative agent of anthracnose that affects economically important crop species (*1*). Furthermore, *Colletotrichum* sp. have recently been reported to cause subcutaneous and systemic infections among immunosuppressed patients (*2*). *Colletotrichum* sp. are facultative biotrophs. Before the fungal hyphae can successfully penetrate and gain access to host tissue, the fungus has to first evade plant antimicrobial hydrolases such as chitinases and β-(1,3)glucanases (*3*, *4*). The chitinases degrade fungal chitin, an insoluble linear polymer of β-(1−4)-linked *N*-acetylglucosamine (GlcNAc).[1] The breakdown products may act as elicitors of active defense responses within the plant (*5*−*7*). Studies of cell wall composition of invasive fungal hyphae suggest that exposed fungal chitin polymers are partially de-N-acetylated during infection and initial growth within the host (*8*). Chitosan, the de-*N*-acetylated product, is a poor substrate for chitinases, which require the presence of *N*-acetyl moieties for recognition and catalysis (*9*). Thus, conversion of chitin to chitosan during plant extracellular colonization may protect pathogenic fungal hyphae from being lysed by secreted plant chitinases. The enzyme responsible for chitin modification is a developmentally regulated, secreted, chitin deacetylase (CDA) (*10*). *C. lindemuthianum* chitin deacetylase (*Cl*CDA) is a member of the family 4 carbohydrate esterases (CE-4s) as defined by the CAZY database [http://afmb.cnrs-mrs.fr/~cazy/CAZY (*11*)], which include several members that share the primary structure assigned as the "NodB homology domain" (*12*). Rhizobial NodB (EC 3.5.1.−) is involved in de-*N*-acetylating the nonreducing end GlcNAc from short chito-oligosaccharides (*13*, *14*) involved in synthesis of Nod factors, which act as morphogenic signal molecules to symbiotic leguminous plant roots. Another large group in the CE-4 family are the peptidoglycan deacetylases (EC 3.1.1.−) that modify bacterial cell wall peptidoglycan by de-*N*-acetylation of either the *N*-acetylmuramic acid (MurNAc) or GlcNAc residues of the disugar repeats. MurNAc deacetylation in *Bacillus subtilis* is carried out by *Bs*PdaA that facilitates the formation of muramic δ-lactam, which is required for germination lytic enzyme recognition (*15*, *16*). *Streptococcus pneumoniae* peptidoglycan deacetylase A (*Sp*PgdA) de-*N*-acetylates

[†] We thank the European Synchrotron Radiation Facility (Grenoble, France) for time at beamline ID14-1. This work was supported by a Wellcome Trust Senior Research Fellowship and the European Union FP6 STREP Fungwall Programme.

[‡] Coordinates and structure factors have been deposited with the PDB (accession code 2iw0).

* Corresponding author. E-mail: dava@davapc1.bioch.dundee.ac.uk. Phone: ++44 1382 344979. Fax: ++ 44 1382 345764.

[§] University of Dundee.

[||] University of British Columbia.

[⊥] Université Paris-Sud.

[#] National Food Research Institute.

[1] Abbreviations: *Cl*CDA, *Colletotrichum lindemuthianum* chitin de-*N*-acetylase; CE-4, family 4 carbohydrate esterase; GlcNAc, *N*-acetylglucosamine; MurNAc, *N*-acetylmuramic acid; *Sp*PgdA, *Streptococcus pneumoniae* peptidoglycan deacetylase A.

10.1021/bi0606694 CCC: $33.50
Published on Web 07/15/2006

GlcNAc sugars of peptidoglycan. Consistent with this, Δ*pgda* strains are hypersensitive to exogenous lysozyme and exhibit significantly less virulence within mouse models (*17*, *18*). Chitin deacetylases (EC 3.5.1.41) have been characterized from several sources: *Mucor rouxii* (*19*, *20*), *Aspergillus nidulans* (*21*), *Absidia coerulea* (*22*), two strains of *C. lindemuthianum* (*23*, *24*), and *Saccharomyces cerevisiae* (*25*, *26*). It has also been demonstrated that *S. cerevisiae* CDA-deficient strains show reduced ascospore wall rigidity and increased susceptibility to lytic enzymes (*26*). Recombinant *Cl*CDA has previously been expressed in *Escherichia coli* (*27*) and recently in *Pichia pastoris* (*28*). *Cl*CDA is a representative member of the CE-4 family and shares a number of sequence motifs, covering several conserved histidine and aspartic acid residues (Figure 1B). It appears from several kinetic studies that divalent cations may play a role in catalysis (*12*, *19*, *28*, *29*). Previous studies have shown that *Cl*CDA is an endo-chitin deacetylase with four significant subsites, −2,−1, 0, and +1 (where 0 is the catalytic site), and that subsites −2 and 0 strongly recognize the *N*-acetyl groups on the GlcNAc sugars whereas subsite +1 recognizes a glucosamine moiety (*30*−*32*). These studies have suggested that chitin is only partially deacetylated in a specific manner that may prevent recognition by either chitinases or chitosanases. The first structure of a CE-4 family member, *B. subtilis* PdaA, was reported recently (*33*). The protein adopts a $(\beta/\alpha)_8$ fold with a putative substrate-binding groove harboring the majority of the conserved residues. The data obtained from soaking studies proved inconclusive as to possible metal/substrate-binding sites. A more recent structural study of the CE-4 member *Sp*PgdA (*34*) reveals that its catalytic domain shows the same conserved groove but also revealed a zinc ion coordinated by a conserved zinc-binding triad consisting of His-His-Asp. These residues are highly conserved throughout the CE-4 family. Mutagenesis studies in combination with kinetic data on metal-dependent activity showed that *Sp*PgdA uses a metal-dependent mechanism involving acid/base catalysis similar to other zinc-dependent de-*N*-acetylases (*34*). Furthermore, the structures of two bacterial acetylxylan esterases from *Streptomyces lividans* (*Sl*CE4) and *Clostridium thermocellum* (*Ct*CE4) have recently been described in conjunction with compelling biochemical data that implicates these esterases as metal dependent with a preference for Co^{2+} (*35*). Here, we present the structure of a recombinant chitin de-*N*-acetylase from *C. lindemuthianum* (*Cl*CDA), the first "fungal member of the CE-4 family" to be structurally determined, which retains the classical His-His-Asp Zn^{2+} coordination observed previously. We use X-ray crystallography, enzymology, subsite probing, inductively coupled plasma mass spectrometry, atomic spectroscopy, and ligand modeling to define the structure and investigate the reaction mechanism and substrate binding of *Cl*CDA.

MATERIALS AND METHODS

Crystallization, Structure Solution, and Refinement. Recombinant C-terminal hexa-His-tagged *Cl*CDA protein was cloned from *C. lindemuthianum* UPS9 strain (GenBank accession number AY633657), expressed, and purified from *P. pastoris* as described previously (*28*). The purified protein was stored at −80 °C in Tris-HCl (30 mM, pH 8.0) before being defrosted on ice. The purity was assessed by SDS−PAGE. The pure *Cl*CDA protein was crystallized using sitting drop vapor diffusion by mixing 1 μL of protein solution (20 mg/mL in buffer) with the same volume of mother liquor solution [30% (w/v) PEG 4000, 0.2 M ammonium acetate, and 0.1 M sodium acetate, pH 4.6]. The protein forms platelike crystals that grow at 20 °C within 10 days. Crystals were soaked in mother liquor supplemented with 10 mM $ZnCl_2$ for 3 h, then cryoprotected in mother liquor containing 15% glycerol, and flash frozen in a nitrogen gas stream cooled to 100 K. Data were collected at beam line ID14-1 at the European Synchrotron Radiation Facility in Grenoble. Data were integrated and scaled using the program HKL2000 (*36*). The *Cl*CDA structure was solved by molecular replacement using MOLREP (*37*) with the previously solved *Sp*PgdA C-terminal catalytic core (residues 268−463) [Protein Data Bank code 2C1G (*34*)] as a search model. A single solution was found with an *R*-factor of 0.559 and a correlation coefficient of 0.278. The resulting model phases were then used for automated model building with WarpNtrace (*38*), which was able to build 211 out of 255 residues. The resulting model was refined using CNS (*39*) and REFMAC (*40*); model building was carried out with O (*41*) and Coot (*42*). After several rounds of refinement the electron density maps indicated that two residues (125 and 126) were different from the published sequence for *Cl*CDA (UPS9 strain). It appeared that these residues followed the sequence of the *Cl*CDA ATCC strain, and they were refined as Gln125 and Leu126. These residues are indicated in Figure 1B with stars and are both solvent exposed. Ligands were only included when unambiguously defined by unbiased $|F_o| - |F_c|$, ϕ_{calc} maps. Ligand topologies and coordinates were generated by PRODRG (*43*), and the figures were made using PyMOL (*44*). Final data and refinement statistics are shown in Table 1.

Table 1: Crystallographic Data[a]

*Cl*CDA	WT zinc acetate
wavelength (Å)	0.931
space group	$P2_12_12$
unit cell (Å)	$a = 71.28$, $b = 55.02$, $c = 60.06$
resolution range (Å)	20.00−1.80 (1.86−1.80)
no. of observed reflections	474363
no. of unique reflections	22257 (2181)
redundancy	6.0 (6.1)
$I/\sigma I$	25.4 (2.9)
completeness (%)	99.9 (100.0)
R_{merge}	0.071 (0.518)
R, R_{free}	0.172, 0.215
no. of protein residues	226
no. of water molecules	175
no. of ligands	Zn^{2+}, 3 acetate, PO_4^{3-}, Cl^-
RMSD from ideal geometry	
bonds (Å)	0.021
angles (deg)	1.722
B-factor RMSD (Å^2)	
backbone bonds	1.032
$\langle B \rangle$ (Å^2)	
protein	28.0
ligands	44.2
water	35.1

[a] Details of data collection and structure refinement. Values in parentheses are for the highest resolution shell. All data were included in structure refinement.

Ligand Docking. Computational docking of a GlcNAc trimer with the central sugar forming the predicted oxyanion intermediate was performed with AutoDock 3.0 (*45*). The

*Cl*CDA structure was protonated using the HB2 module of WHAT IF (*46*), yielding a receptor with a protonated Asp49 and a doubly protonated His206 in accordance with the proposed reaction mechanism. Coordinates and topology of the ligand were produced with PRODRG (*43*); the pyranose rings were generated in a $^4C_1$ chair conformation.

Enzymology. The C-terminal hexa-His-tagged *Cl*CDA protein expressed in *P. pastoris* was assayed using the fluorogenic labeling method previously described (*34*). Standard reactions consisted of 100 nM protein (dialyzed into doubly distilled H_2O), 50 mM Bis-Tris, pH 7, and 0.6 mM $(GlcNAc)_3$ in a total volume of 50 μL, incubated for 10 min at 37 °C. The production of free amine was followed by labeling with fluorescamine and quantified with a glucosamine standard. All measurements were carried out in triplicate. The fluorescence intensity data were analyzed by nonlinear regression analysis with GraFit (*47*) using the default equations for first-order reaction rates and Michaelis−Menten steady-state kinetics.

Recombinant C-terminally hexa-His-tagged *Cl*CDA protein was also expressed and purified from *E. coli* as described previously (*31*). Initial rates of hydrolysis by *Cl*CDA were determined at 30 °C with a continuous spectrophotometric assay by following the rate of decrease in absorbance at 216 nm as described previously (*31*). *N*′-Halo-$(GlcNAc)_4$ in 20 mM $Na_2B_4O_7$/HCl, pH 8.5, was preincubated for 10 min at 30 °C, and reaction was initiated by the addition of *Cl*CDA such that the final concentrations in the assays were as follows: 0.01−0.4 mM *N*′-fluoro-$(GlcNAc)_4$ in the presence of 0.658 μg mL^{-1} *Cl*CDA, 0.01−0.4 mM *N*′-chloro-$(GlcNAc)_4$ in the presence of 0.863 μg mL^{-1} *Cl*CDA, and 0.01−0.4 mM *N*′-bromo-$(GlcNAc)_4$ in the presence of 1.08 μg mL^{-1} *Cl*CDA. The plots of initial rates versus substrate concentrations were hyperbolic, and the values of K_m and V_{max} were determined by fitting the initial velocity curves to the standard Michaelis−Menten equation by nonlinear regression using the program GraFit. The k_{cat} values were calculated using a $\Delta\epsilon_{216}$ of 351, 347, and 396 M^{-1} cm^{-1} for *N*′-fluoro-, *N*′-chloro-, and *N*′-bromo-$(GlcNAc)_4$, respectively.

Electrospray Ionization Mass Spectrometry (ESI-MS). ESI-MS was performed, and the spectra were recorded as described previously (*31*).

Inductively Coupled Plasma Mass Spectrometry (ICP-MS). A sample of *Cl*CDA was extensively dialyzed against deionized water and then shown to be catalytically active. The protein concentration was determined using the Micro BCA protein assay reagent kit with BSA standards (Pierce, Rockford, IL). The *Cl*CDA sample and a control sample (deionized water from the dialysis solution) were then analyzed by ICP-MS for the presence of divalent metal ions. ICP-MS was performed at the Pacific Centre for Isotopic and Geochemical Research (PCIGR) at the University of British Columbia (UBC). The accurate zinc concentrations in the *Cl*CDA sample and the control were determined using the method of standard-zinc additions. Calibration curves were constructed by linear regression.

Graphite Furnace Atomic Absorption Spectroscopy (GF-AAS). The same *Cl*CDA sample and the control which were analyzed by ICP-MS (above) were also analyzed by GF-AAS for the presence of atomic zinc (λ_{max} = 213.9 nm). GF-AAS was also performed at the PCIGR at UBC. The accurate zinc concentrations in the *Cl*CDA sample and the control were determined using the method of standard-zinc additions. Calibration curves were constructed by linear regression.

*Synthesis. (A) 2-Acetamido-2-deoxy-β-*D*-glucopyranosyl-(1→4)-2-acetamido-2-deoxy-β-*D*-glucopyranosyl-(1→4)-2-amino-2-deoxy-β-*D*-glucopyranosyl-(1→4)-2-acetamido-2-deoxy-*D*-glucose.* GlcNAcGlcNAcGlcNGlcNAc was synthesized via *Cl*CDA-catalyzed regioselective monodeacetylation of chitotetraose. Chitotetraose (200 mg, 240 μmol) was dissolved in H_2O (2.4 L) so that the final concentration was 0.1 mM (=K_m value). The solution pH was adjusted to 8.5 by addition of NaOH, and *Cl*CDA was added to a final concentration of 2.0 μg mL^{-1}. The solution was stirred at room temperature until full monodeacetylation was achieved as checked by ESI-MS. The reaction was then stopped by boiling for 5 min. The solvent was evaporated, and the residue (170 mg, 90%) was dried under vacuum and used directly in the next step. R_f = 0.13 (5:5:2.5:0.2 2-propanol/EtOH/H_2O/NH_4OH). ESI-MS: calcd for *m*/*z* $[M + Na]^+$, 811.3; found, 811.5. The position of deacetylation was confirmed via ESI-MS analysis of the *β-N*-acetylhexosaminidase hydrolysate of GlcNAcGlcNAcGlcNGlcNAc.

*(B) 2-Acetamido-2-deoxy-β-*D*-glucopyranosyl-(1→4)-2-acetamido-2-deoxy-β-*D*-glucopyranosyl-(1→4)-2-deoxy-2-fluoroacetamido-β-*D*-glucopyranosyl-(1→4)-2-acetamido-2-deoxy-*D*-glucose.* Dicyclohexylcarbodiimide (9.3 mg, 45 μmol) in dry pyridine (1 mL) was added slowly to a solution of GlcNAcGlcNAcGlcNGlcNAc (24 mg, 30 μmol) and sodium fluoroacetate (4.2 mg, 42 μmol) in dry DMF (10 mL) under N_2 atmosphere at room temperature. The solution was stirred overnight, then the solvent was evaporated, and the residue was purified by normal-phase HPLC (Waters chromatography system; Millipore Co.). The sample was loaded onto an HPLC column (2.15 × 30.0 cm, TSK-GEL Amide-80; Tosoh Co.), and the product was eluted with a linear gradient of 100% CH_3CN to 50% CH_3CN in water at a flow rate of 5 mL min^{-1} (8.9 mg, 35%). R_f = 0.65 (5:5:2.5:0.2 2-propanol/EtOH/H_2O/NH_4OH). ^{1}H NMR (400 MHz, D_2O): δ 1.93−1.95 (m, 9 H, 3 C*H*$_3$CONH), 3.35−3.83 (m, 24 H, H2,2′,2″,2‴,3,3′,3″,3‴,4,4′,4″,4‴,5,5′,5″,5‴,6,6′,6″,6‴), 4.71−4.85 (dm, 2 H, $J_{H,F}$ = 48 Hz, CH_2F), 4.48 (d, J = 8.3 Hz, H1β,1′,1″,1‴), 5.08 (d, J = 1.9 Hz, H1α) ppm. ^{19}F NMR (188.3 MHz, D_2O): δ −152.01 (dm, $J_{H,F}$ = 49 Hz) ppm. ^{13}C NMR (75 MHz, D_2O): δ 22.11, 22.38 (3 *C*H_3CONH); 54.01, 55.35, 55.85, 56.45 (C2,2′,2″,2‴); 60.19, 60.51, 60.60, 60.87 (C6,6′,6″,6‴); 69.51, 70.05, 70.31, 72.17, 72.41, 72.72, 73.77, 74.80, 74.89, 76.23, 79.15, 79.28, 79.50, 79.58 (C3,3′,3″,3‴, C4,4′,4″,4‴, C5,5′,5″,5‴); 80.02 (CH_2F); 90.71, 94.98, 101.10, 101.45, 101.74 (C1,1′,1″,1‴); 170.72 (NH*C*OCH_2F); 174.75, 174.93, 175.07 (3 NH*C*OCH_3) ppm. HR-ESI-MS: calcd for *m*/*z* $[M + Na]^+$, 871.3084; found, 871.3091.

*(C) 2-Acetamido-2-deoxy-β-*D*-glucopyranosyl-(1→4)-2-acetamido-2-deoxy-β-*D*-glucopyranosyl-(1→4)-2-chloroacetamido-2-deoxy-β-*D*-glucopyranosyl-(1→4)-2-acetamido-2-deoxy-*D*-glucose.* Chloroacetic anhydride (0.26 g, 1.52 mmol) was added slowly over a period of 10 h to a solution of GlcNAcGlcNAcGlcNGlcNAc (24 mg, 30 μmol) and Et_3N (10 μL, 72 μmol) in dry MeOH (25 mL) under a N_2 atmosphere at room temperature. The solution was stirred for an additional 24 h, then the solvent was evaporated, and

the residue was purified by normal-phase HPLC as described above (12 mg, 46%). R_f = 0.66 (5:5:2.5:0.2 2-propanol/EtOH/H_2O/NH_4OH). ^{1}H NMR (400 MHz, D_2O): δ 2.06−2.08 (m, 9 H, 3 C*H*$_3$CONH), 3.48−3.95 (m, 24 H, H2,2′,2″,2‴,3,3′,3″,3‴,4,4′,4″,4‴,5,5′,5″,5‴,6,6′,6″,6‴), 4.21−4.22 (m, 2 H, CH_2Cl), 4.60 (d, J = 8.3 Hz, H1β,1′,1″,1‴), 5.21 (d, J = 1.8 Hz, H1α) ppm. ^{13}C NMR (75 MHz, D_2O): δ 22.19, 22.42 (3 *C*H_3CONH); 42.54 (CH_2Cl); 53.99, 55.33, 55.89, 56.49 (C2,2′,2″,2‴); 60.25, 60.49, 60.59, 60.85 (C6,6′,6″,6‴); 69.50, 70.02, 70.28, 72.19, 72.45, 72.73, 73.75, 74.82, 74.88, 76.22, 79.13, 79.25, 79.51, 79.60 (C3,3′,3″,3‴, C4,4′,4″,4‴, C5,5′,5″,5‴); 90.75, 95.12, 101.04, 101.55, 101.77 (C1,1′,1″,1‴); 170.58 (NH*C*OCH_2Cl), 174.77, 174.92, 175.05 (3 NH*C*OCH_3) ppm. HR-ESI-MS: calcd for m/z [M + Na]$^+$, 887.2788; found, 887.2800.

*(D) 2-Acetamido-2-deoxy-β-*D*-glucopyranosyl-(1→4)-2-acetamido-2-deoxy-β-*D*-glucopyranosyl-(1→4)-2-bromoacetamido-2-deoxy-β-*D*-glucopyranosyl-(1→4)-2-acetamido-2-deoxy-*D*-glucose.* Bromoacetic anhydride (0.20 g, 0.77 mmol) was added slowly over a period of 24 h to a solution of GlcNAcGlcNAcGlcNGlcNAc (30 mg, 38 μmol) and Et_3N (10 μL, 72 μmol) in dry MeOH (15 mL) under a N_2 atmosphere at room temperature. The solution was stirred for an additional 48 h, then the solvent was evaporated, and the residue was purified by normal-phase HPLC as described above (16 mg, 46%). R_f = 0.67 (5:5:2.5:0.2 2-propanol/EtOH/H_2O/NH_4OH). ^{1}H NMR (400 MHz, D_2O): δ 1.86−1.89 (m, 9 H, 3 C*H*$_3$CONH), 3.26−3.76 (m, 24 H, H2,2′,2″,2‴,3,3′,3″,3‴,4,4′,4″,4‴,5,5′,5″,5‴,6,6′,6″,6‴), 3.77−3.78 (m, 2 H, CH_2Br), 4.40 (d, J = 8.3 Hz, H1β,1′,1″,1‴), 5.01 (d, J = 2.0 Hz, H1α) ppm. ^{13}C NMR (75 MHz, D_2O): δ 21.90, 22.13 (3 *C*H_3CONH); 27.94 (CH_2Br); 53.72, 55.04, 55.60, 56.23 (C2,2′,2″,2‴); 60.02, 60.26, 60.34, 60.57 (C6,6′,6″,6‴); 69.16, 69.74, 69.97, 71.97, 72.16, 72.39, 73.46, 74.52, 74.59, 74.82, 75.92, 78.39, 78.88, 79.01, 79.23 (C3,3′,3″,3‴, C4,4′,4″,4‴, C5,5′,5″,5‴); 90.75, 95.12, 101.04, 101.55, 101.77 (C1,1′,1″,1‴); 170.44 (NH*C*OCH_2Br), 174.47, 174.61, 174.75 (3 NH*C*OCH_3) ppm. HR-ESI-MS: calcd for m/z [M + Na]$^+$, 931.2284; found, 931.2261.

RESULTS

ClCDA Structure and Active Site Groove. The chitin deacetylase was crystallized, synchrotron diffraction data were collected to 1.8 Å, and the structure was solved by molecular replacement using the recently published *Sp*PgdA C-terminal domain (residues 268−463) structure as a search model (*34*), followed by refinement to a final *R*-factor of 0.172 (R_{free} = 0.215, Table 1). The *Cl*CDA structure reveals a compact single catalytic domain similar to the deformed $(\beta/\alpha)_8$ fold adopted by other CE-4 family members (Figure 1A). Superposition on the *Sp*PgdA structure (*34*) yields an RMSD of 1.35 Å on 179 equivalenced Cα atoms (Figure 1A). Nevertheless, there are significant topological differences between *Cl*CDA, the C-terminal domain of *Sp*PgdA, and *Bs*PdaA (Figure 1A). The *Cl*CDA N/C-termini are on the same side of the barrel, while in *Sp*PgdA and *Bs*PdaA the N/C-termini are located at opposite ends. The first strand of *Cl*CDA (β1) and equivalent *Bs*PdaA (β2) is topologically equivalent to the final strand of the barrel in *Sp*PgdA (β17, Figure 1A). Indeed, so far all of the structurally defined members of the CE-4 family adopt a degree of "secondary structure swapping" from the canonical CE-4 $(\beta/\alpha)_8$ fold. The solvent-exposed active site cleft of the protein is formed from the C-terminal ends of β-strands 2, 4, 5, 7, and 8 of the $(\beta/\alpha)_8$ barrel and includes the five distinct sequence motifs conserved in CE-4 family members (MT1−MT5 in Figures 1B and 2) (*34*). The most notable difference in the architecture of the catalytic groove compared to other family members is the presence of an extended loop between strand β3 and helix α2 supporting a solvent-exposed Trp79 that protrudes into the catalytic cleft (Figures 1B and 2A). The *Cl*CDA structure also reveals two intramolecular disulfide bonds that may add stability to this secreted protein but are absent from the homologous bacterial *Sp*PgdA and *Bs*PdaA that deacetylate peptidoglycan within the bacterial cell wall. Sequence alignment suggests that one disulfide (Cys38-Cys237), tethering the N-terminal and C-terminal ends of the structure, is also conserved in the fungal chitin deacetylase from *M. rouxii* (Figure 1). Further, the tethering of the N- and C-terminal ends in this fashion appears to be common from extensive sequence alignments (not shown) in other CE-4 family members. Although many of the cysteines do not align directly with the *Cl*CDA sequence, the recently solved structure of *Sl*CE-4 reveals a disulfide linkage tethering the N- and C-terminal ends in this fashion (Figure 1B) (*35*). The other disulfide (Cys148-Cys152) (Figure 1) appears to compensate for the difference in length between the α4 helix of *Cl*CDA and the three residue shorter *Sp*PgdA equivalent, by pinning back the loop containing MT3 to the elongated α4 helix. This places the loop and hence MT3 into a conformation similar to that of *Sp*PgdA, forming one of the sides of the active site groove (Figure 2A). MT4 forms the other side of the active site groove. Compared to *Sp*PgdA, it contains two significant substitutions overhanging the catalytic cleft, a lysine (Lys171) and a tyrosine (Tyr173) replacing a leucine and a solvent-exposed tryptophan, respectively (Figure 2A).

The Active Site Shows a Conserved Metal-Binding Triad. The catalytic groove is similar to that of *Sp*PgdA and *Sl*CE4 (*35*) with the catalytic subsite being generated by a zinc-binding triad consisting of two histidines (His104, His108) from motif 2 and an aspartic acid (Asp50) from motif 1. This His-His-Asp metal-binding triad is conserved throughout the CE-4 family, with the exception of *Bs*PdaA and the recently characterized xylan esterase *Ct*CE4 (*35*), which only have two metal coordinating residues. The *Cl*CDA electron density map reveals a large peak (30σ in difference map), presumed to be zinc, coordinated by the metal-binding triad. The structure also contains a well-ordered acetate ion (7.5σ peak in the difference map) in a position similar to that observed in the *Sp*PgdA−acetate complex (Figure 2B). Thus, the zinc ion is coordinated in an octahedral fashion by two histidines, an aspartic acid, a water molecule, and a bidentate interaction with the acetate molecule. One of the acetate oxygens interacts with Asp49 (MT1), which in turn is tethered by a buried Arg142 (MT3). The same oxygen is also within 3.35 Å of His206 (MT5) that interacts with Asp172 (MT4) (Figure 2A). The backbone nitrogen from Tyr145 (MT3) forms a hydrogen bond with the other acetate oxygen. These residues are conserved not only at the sequence level (Figure 1B) but also at the structural level with equivalent *Sp*PgdA residues (Figure 2B). Motif 5 also contains a conserved leucine (Leu204) that in combination with a nonconserved leucine (Leu146) from MT3 forms a

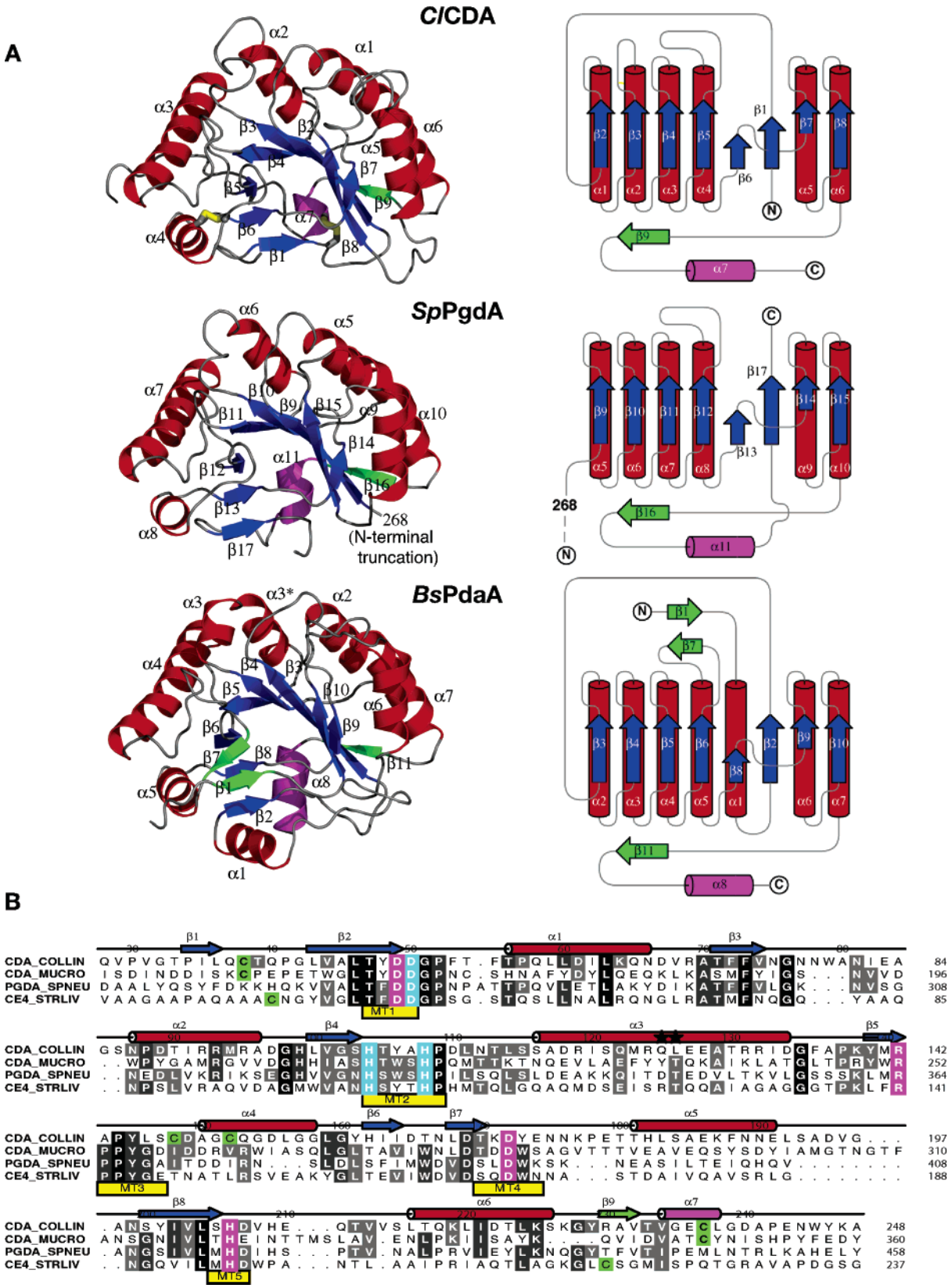

FIGURE 1: (A) *Cl*CDA structure. Ribbon drawing of the structures of *Cl*CDA, C-terminal domain of *Sp*PgdA (residues 268−463) (PDB entry 2c1g), and *Bs*PdaA (PDB entry 1w17), alongside topological representations as constructed with TopDraw (*53*). Helices are colored red and strands blue, except for helices and strands which do not fit the canonical β/α fold. Secondary structure elements for *Cl*CDA are named as indicated in the sequence alignment in panel B, and the two disulfide bonds are colored yellow. (B) Sequence alignment of CE-4 family members. The sequences of four representative family 4 carbohydrate esterases are shown: CDA_COLLIN, *C. lindemuthianum* chitin deacetylase; CDA_MUCRO, *M. rouxii* chitin deacetylase; PGDA_SPNEU, *S. pneumoniae* PgdA; CE4_STRLIV, *S. lividans* xylan esterase. The five CE-4 motifs (MT1−5, yellow), the metal ligands (cyan), the catalytic residues (magenta), and the cystines (green) are indicated. The black stars indicate the amino acid changes from the *C. lindemuthianum* UPS9 strain sequence. The sequences are aligned on the basis of the respective experimental structures, with the exception of CDA_COLLIN for which no structure is available. Sequence manipulation was carried out using Aline 1.0 (Charlie Bond, personal comunication).

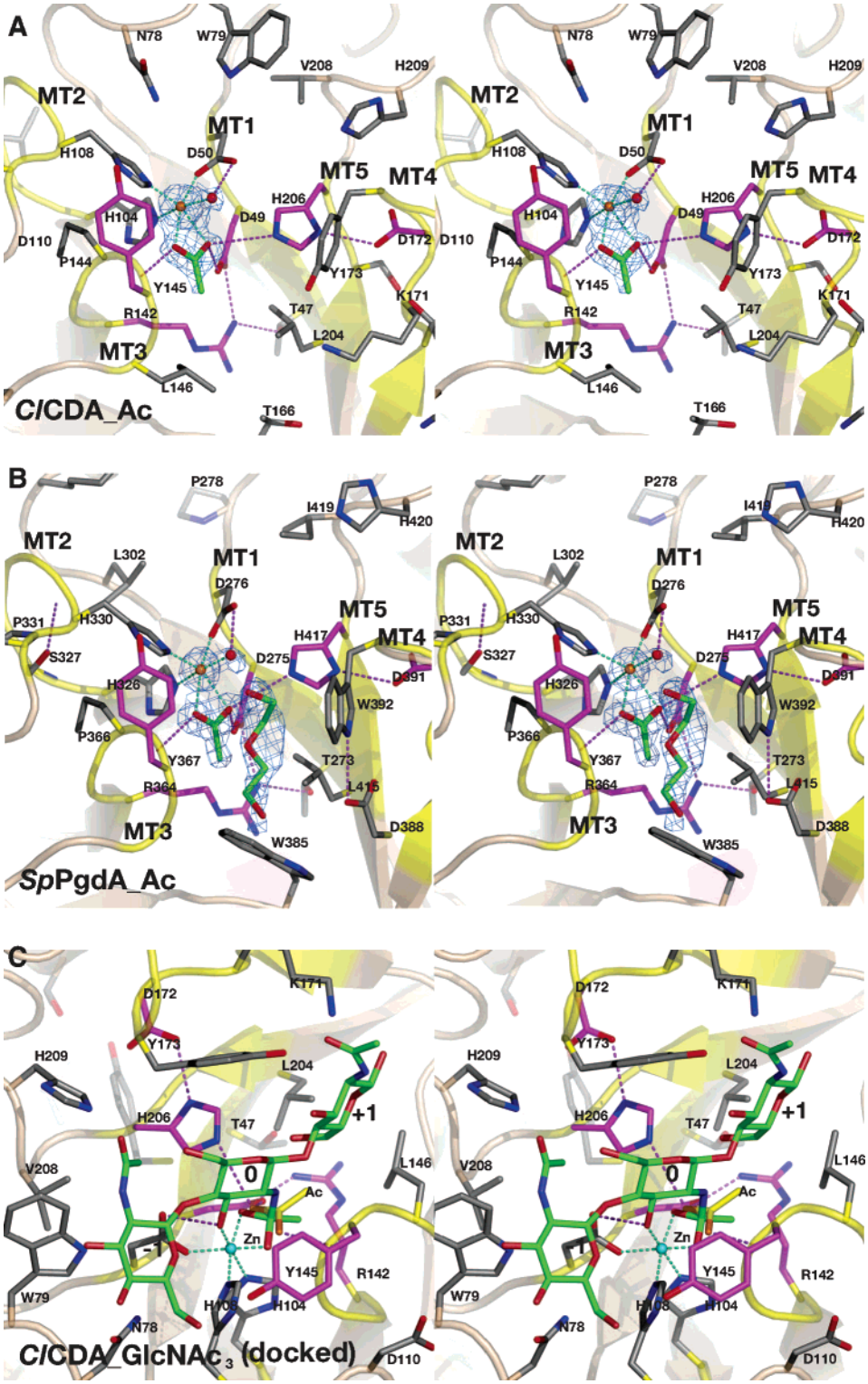

FIGURE 2: Details of the *Cl*CDA active site. Close up of the active sites of the native *Cl*CDA structure in complex with acetate product (panel A, *Cl*CDA_Ac), *Sp*PgdA in complex with acetate (panel B, *Sp*PgdA_Ac) (acetate and PEG molecules shown as sticks with green carbons), and a docked $GlcNAc_3$ complex [panel C, *Cl*CDA_$GlcNAc_3$ (docked)]. Ribbon diagrams of the active sites are shown, with conserved side chains shown as sticks with magenta carbons. The experimentally observed acetate is shown as sticks with yellow carbons. $GlcNAc_3$ is shown as green sticks with subsites labeled −1, 0, and +1. The five CE-4 sequence motifs (MT1−5) are shown in yellow. Water molecules (red spheres) are also shown. Unbiased $|F_o| - |F_c|$, ϕ_{calc} maps are shown in blue. Hydrogen bonds are shown in dashed magenta lines (*Cl*CDA Tyr145 and *Sp*PgdA Tyr367 backbone nitrogen atoms are not shown) and zinc−ligand interactions as dashed cyan lines.

hydrophobic patch that appears to accommodate the acetate methyl group. This is not dissimilar to the corresponding pocket of *Sp*PgdA, which utilizes a tryptophan from the N-terminal end of MT4 to occupy a similar position to that of Leu146 (Figure 2A,B).

Intermolecular Interactions of the Histidine Tag with the Active Site. During refinement, it became apparent that there was a significant amount of uninterpreted electron density in the catalytic groove of the protein. This density was resolved to be the C-terminal hexahistidine purification tag.

Table 2: Steady-State Kinetic Parameters for *Cl*CDA Expressed in *E. coli*, Assayed Using Direct Continuous Spectrophotomeric Assay,[a] and *Cl*CDA Expressed in *P. pastoris*, Assayed Using Fluorogenic Labeling Method[b] with Respect to $(GlcNAc)_{2-4}$ and *N*′-Halo-$(GlcNAc)_4$ Substrates

substrate	K_m (mM)	k_{cat} (s^{-1})	k_{cat}/K_m ($mM^{-1}\cdot s^{-1}$)
$(GlcNAc)_2$[a]	18 ± 2	11 ± 2	0.6 ± 0.2
$(GlcNAc)_3$[b]	0.66 ± 0.05	1.53 ± 0.041	2.3 ± 0.8
$(GlcNAc)_3$[a]	4.3 ± 0.1	6 ± 1	1.4 ± 0.4
$(GlcNAc)_4$[a]	0.125 ± 0.007	7 ± 2	56 ± 13
N′-bromo-$(GlcNAc)_4$[a]	0.102 ± 0.004	31 ± 3	304 ± 32
N′-chloro-$(GlcNAc)_4$[a]	0.18 ± 0.03	47 ± 5	261 ± 52
N′-fluoro-$(GlcNAc)_4$[a]	0.14 ± 0.02	68 ± 6	486 ± 82

[a] Direct continuous spectrophotomeric assay. [b] Fluorogenic labeling method.

Strikingly, this appeared to be an intermolecular interaction, with the C-terminus of one molecule extending into the active site of one of the symmetry-related molecules. The hexahistidine tag appears to make several interactions; the carboxyl oxygen from the C-terminal His254 is in hydrogen-bonding distance of His206 Nϵ2 at 2.5 Å and the water molecule closest to the Zn^{2+} at 2.6 Å. Tyr145 stacks with His251, Asp110 hydrogen bonds with His251 Nϵ2 at 2.9 Å, and several water-mediated hydrogen bonds can also be seen. To confirm that the His-tagged recombinant *Cl*CDA protein expressed in *P. pastoris* used for crystallization is active, a fluorescence-based assay was used to verify the activity with $(GlcNAc)_3$ revealing that *Cl*CDA initial velocity measurements with increasing substrate concentration fitted Michaelis−Menten kinetics. The K_m was determined to be 0.66 ± 0.05 mM with a k_{cat} of 1.53 ± 0.04 s^{-1} (Table 2). These values are in keeping with the results previously reported for *Cl*CDA expressed in *E. coli* and assayed using a direct, continuous spectrophotometric assay (*31*) that gave a K_m of 4.3 ± 0.1 mM and a k_{cat} of 6 ± 1 s^{-1} for $(GlcNAc)_3$ (Table 2).

ClCDA Tightly Binds Zinc. Previous experiments on *Sp*PgdA (*34*) and xylan esterases (*35*) have shown that activity of these CE-4 esterases is dependent on the presence of a divalent cation, preferably cobalt or zinc. Strikingly, however, the recombinant *Cl*CDA proteins from both *P. pastoris* and *E. coli* were not inhibited by the metal chelator ethylenediaminetetraacetic acid (EDTA), nor was there any significant increase in catalytic activity in the presence of either of the divalent cations Co^{2+}, Zn^{2+}, Cd^{2+}, Cu^{2+}, Ni^{2+}, Fe^{2+}, Mn^{2+}, Mg^{2+}, or Ca^{2+} (data not shown). We therefore attempted to directly detect the presence of a tightly bound divalent cation in the recombinant protein. Inductively coupled plasma mass spectrometric (ICP-MS) analysis showed a higher level of elemental zinc in the *Cl*CDA sample (dialyzed in deionized water) relative to the control (deionized water). The accurate zinc concentrations in the *Cl*CDA sample and the control were then determined by ICP-MS analysis using the method of standard-zinc additions. After correction for the background zinc concentration in the control, the zinc content of *Cl*CDA was calculated to be 0.8 zinc atom per *Cl*CDA molecule. We also determined the accurate zinc concentrations in the same *Cl*CDA sample and the control by another independent method, namely, graphite furnace atomic absorption spectroscopy (GF-AAS), using the method of standard-zinc additions. After background correction, this method rendered a zinc content of 0.7 zinc atom per *Cl*CDA molecule. Hence, the presence of a tightly enzyme-bound zinc ion is confirmed by two independent analytical methods in agreement with the structural observations. This zinc ion must be so tightly bound to the enzyme active site that it does not equilibrate with solution, hence the lack of *Cl*CDA inhibition by EDTA.

ClCDA Catalysis Proceeds through a Tetrahedral Oxyanion Intermediate. Previous structural and mutagenesis studies have suggested that CE-4 esterases use a general acid/base catalytic mechanism involving an activated water molecule, much like that observed for other zinc-dependent hydrolases and probably involving a tetrahedral oxyanion intermediate (*34*). To study the precise nature of the reaction intermediate, we have investigated the hydrolysis of *N*′-halo-$(GlcNAc)_4$ derivatives. *Cl*CDA-catalyzed hydrolysis of the *N*′-haloacetamido groups of *N*′-halo-$(GlcNAc)_4$ derivatives (fluoro, chloro, bromo) in the assay buffer at 30 °C and pH 8.5 was studied under steady-state conditions by continuous monitoring of the decrease in A_{216} over time. Initial rates for all of these substrate analogues followed Michaelis−Menten kinetics, and the average values of the observed kinetic parameters k_{cat}, K_m, and (k_{cat}/K_m) were determined (Table 2). The K_m values for all three compounds were similar to that of $(GlcNAc)_4$, suggesting that the haloacetyl group can fit in the active site without any significant steric hindrance (assuming K_m approximates K_s). However, the k_{cat} values increased with the increasing electron-withdrawing ability of the halogen substituent. ESI-MS analysis within the steady-state time scale confirmed that the only product was (GlcNAcGlcNAcGlcNGlcNAc), indicating that the kinetic parameters solely represent hydrolysis at the *N*′ position (Figure 3E), as previously found with the $(GlcNAc)_4$ substrate (*31*). The rates of nucleophilic attack on the carbonyl carbon of amides/esters are known to increase with electron withdrawal in the acyl portion (*48*). This is due to the increase of negative charge along the reaction coordinate from the neutral substrate to the negatively charged tetrahedral intermediate. Hence, electron withdrawal in the acyl portion stabilizes the intermediate relative to the ground state, thereby decreasing the activation energy. Therefore, a plot of log(rate constant) versus substituent constant (σ) should be linear with a positive slope (ρ) based on the Hammett linear free energy correlation (Figure 3C,D) (*49*, *50*). The magnitude of the slope (ρ) is an indication of the extent of charge development in the transition state. A linear relationship was observed (Figure 3F) by plotting log(k_{cat}) versus the Taft substituent constants (σ_1) for H, Br, Cl, and F (*51*, *52*). The values of σ_1 are defined in terms of the pK_a values of the corresponding substituted acetic acids. The presence of a correlation with a positive slope shows that there is a substituent inductive effect in *Cl*CDA-catalyzed hydrolyses of the substituted acetamido groups, indicating the presence of an oxyanion intermediate. The oxyanion intermediate must have a tetrahedral structure in a displacement mechanism. The value of the slope ($\rho = 1.7 \pm 0.3$) indicates significant negative charge development at the transition state. This supports the previously proposed CE-4 esterase reaction mechanism (*34*).

A Predicted $(GlcNAc)_3$ Complex Suggests Exposed −1/+1 N-Acetyl Groups. In the absence of a *Cl*CDA substrate complex, computational docking was carried out using

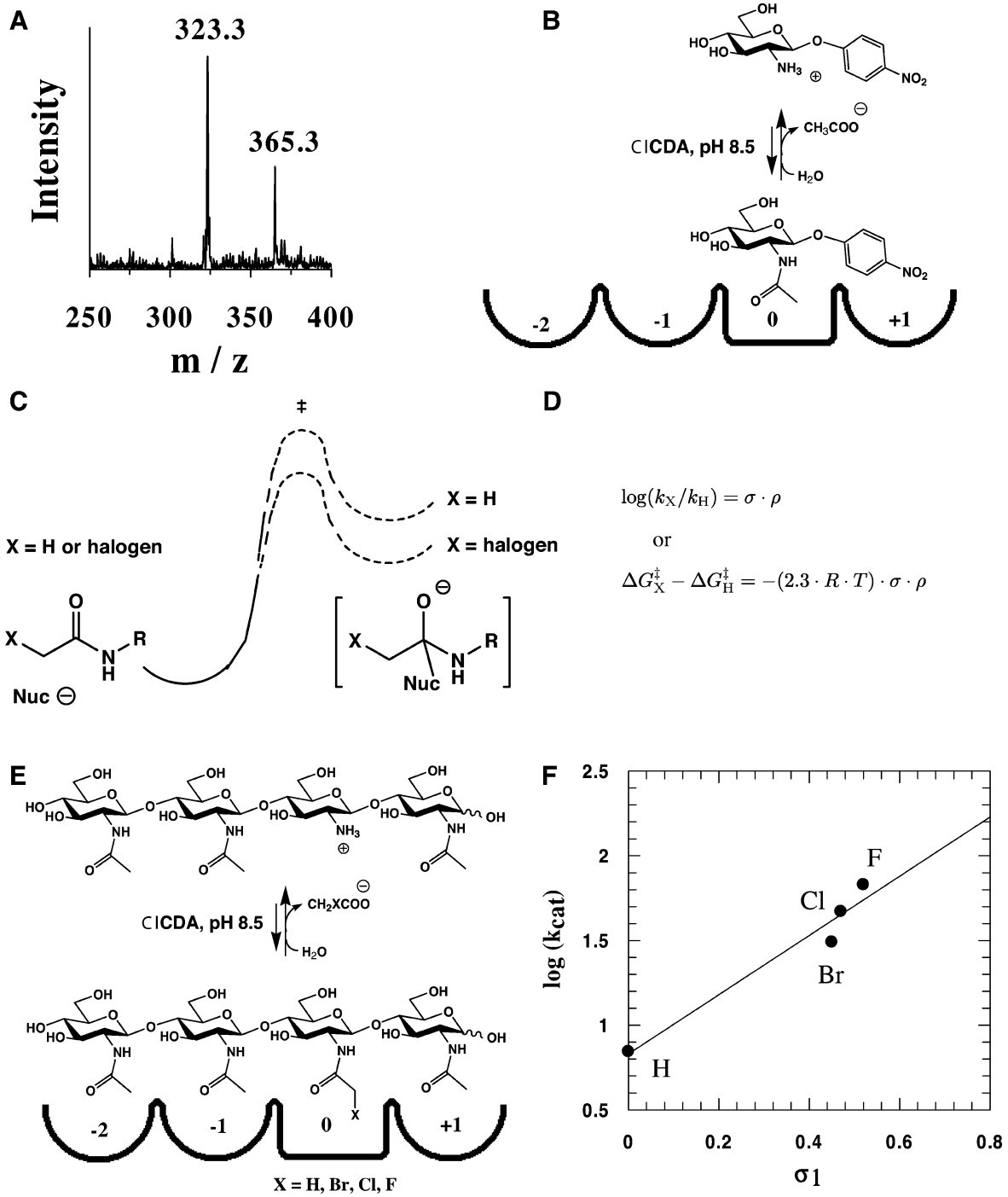

FIGURE 3: *Cl*CDA-catalyzed deacetylation of *p*NP*β*GlcNAc: (A) ESI mass spectrum showing the substrate and the product *p*NP*β*GlcN with a mass difference of 42.0 (CH_3CO minus H); both peaks represent $[M + Na]^+$ species; (B) schematic representation of the productive binding mode of *p*NP*β*GlcNAc to *Cl*CDA. A model for understanding substituent effects in amide hydrolysis: (C) schematic representation of the stabilization of an oxyanion tetrahedral intermediate relative to the ground-state amide by electron withdrawal in the acyl portion; (D) Hammett linear free energy equation. σ is the substituent constant and ρ is the reaction constant. Hammett linear free energy correlation: (E) schematic representation of the productive binding mode of *N*′-halo-$(GlcNAc)_4$ to *Cl*CDA; (F) plot of $\log(k_{cat})$ versus Taft substituent constants (σ_1) for *Cl*CDA-catalyzed hydrolyses of substituted *N*′-acetamido groups of *N*′-halo-$(GlcNAc)_4$ substrates. The line shown is the linear fit of the experimental data (●). The slope (ρ) is 1.7 ± 0.3.

AutoDock (*45*) to place the proposed oxyanion intermediate of $(GlcNAc)_3$ in the catalytic groove. A representative docked complex is shown in Figure 2C. The centrally positioned GlcNAc carrying the oxyanion intermediate is proximal to the zinc, occupying the 0 subsite. Its O3 hydroxyl is seen to interact with the zinc ion and one of the metal ligands (Asp50). The pyranose ring makes hydrophobic interactions with the adjacent aromatic ring of Tyr173 (MT4). The terminal GlcNAc residues occupy the −1 and +1 subsites within the exposed groove. The acetyl group of the GlcNAc occupying the −1 position makes no interactions with the protein, which is in keeping with the findings of Hekmat et al. (*31*). Interestingly, there is a solvent-exposed tryptophan (Trp79) positioned on a nonconserved extended loop that may interact with the proposed −2 subsite binding sugar (Figures 1B and 2). The GlcNAc occupying the +1 subsite is within hydrogen-bonding distance of Lys171 and the hydroxyl of Tyr173. The GlcNAc acetyl group is positioned

in a similar conformation to that of the −1 subsite sugar, pointing out of the catalytic groove. The tetrahedral intermediate is coordinated to the zinc, with the two oxygens and the methyl group similarly positioned to the equivalent atoms in the experimentally determined acetate complex (maximum shift of equivalent atoms is 1.2 Å, Figure 2C). One of the oxygens interacts directly with the zinc ion and the backbone nitrogen of Tyr145, while the other oxygen interacts with the proposed catalytic base Asp49. This arrangement is proposed to be the "oxyanion hole" that stabilizes the developing negative charge on the carbonyl oxygen atom during formation of the tetrahedral intermediate. The nitrogen of the tetrahedral intermediate is within 3.7 Å of the His206 Nϵ2 atom that is presumed to be protonated by the concealed and conserved Asp172 and could therefore act as an acid, protonating the nitrogen in the reaction intermediate, which generates a good leaving group. This hypothesis is generated by the degree of conservation of key catalytic residues between *Cl*CDA and *Sp*PgdA (Figure 2A,B) for which mutagenic analysis has been carried out on equivalent residues in *Sp*PgdA and found to be essential for activity (*34*). From the structural studies, the in silico data, and the reaction mechanism proposed for *Sp*PgdA, it can be proposed that *Cl*CDA de-*N*-acetylates chitin/chito-oligosaccharides by tightly binding a water molecule to the catalytic zinc. The catalytic base Asp49 abstracts a proton from the water molecule, generating a nucleophile to attack the substrate carbonyl carbon. This produces a tetrahedral oxyanion intermediate, the charge of which is stabilized by the metal and the backbone nitrogen of Tyr145. The pK_a-tuned His206 then protonates the reaction intermediate on the nitrogen as it breaks down, generating a free amine and also the acetate product, as seen in the crystal structure (Figure 2A).

Hydrophobic Interactions Are Important for Binding of the +1 Sugar. Previously, Hekmat et al. proposed that *Cl*CDA has four specific sugar-binding subsites (−2, −1, 0, and +1), where subsite 0 represents the site of catalysis. They also found that subsite +1 makes the largest contribution to the overall binding free energy change, although it does not seem to interact with or recognize the *N*-acetyl group of the substrate (*31*). Interestingly, the structure of the docked complex reveals the presence of a solvent-exposed tyrosine (Tyr173, structurally equivalent to Trp392 in the *Sp*PgdA structure, Figure 2A,B) that appears to stack with the +1 sugar. To probe the contribution of such hydrophobic stacking interactions at this subsite, 4-nitrophenyl 2-acetamido-2-deoxy-β-D-glucose (*p*NPβGlcNAc) was tested as a substrate for *Cl*CDA (Figure 3B). Although no *Cl*CDA-catalyzed hydrolysis of GlcNAc was observed at concentrations up to 100 mM, 15 mM *p*NPβGlcNAc was deacetylated slowly at 30 °C and pH 8.5 in the presence of 1.17 μM *Cl*CDA over a time period of days as detected by ESI-MS (Figure 3A). The reaction was therefore more than 2 orders of magnitude slower than that measured with $(GlcNAc)_2$ occupying the same subsites 0 and +1. Kinetic parameters for the reaction were not determined because of the limited solubility of *p*NPβGlcNAc and the impossibility of following the reaction spectrophotometrically in the UV region due to very high absorbance by the aromatic *p*NP group. Nevertheless, the detectable turnover of *p*NPβGlcNAc by *Cl*CDA supports the importance of hydrophobic interactions at subsite +1.

DISCUSSION

The mechanistic studies presented here combined with the structural data show that *Cl*CDA is a zinc-dependent mononuclear metalloenzyme. The crystal structure reveals the previously characterized zinc-binding motif (His-His-Asp) first elucidated in the structure of the Gram-positive bacterial peptidoglycan deacetylase *Sp*PgdA (*34*) and conserved in CE-4 family members with few exceptions. Two "charge relay" side chain pairs are observed, consisting of the catalytic base (Asp49) tethered by a conserved Arg142 and the catalytic acid (His206) tethered by a conserved Asp172, which perform acid/base catalysis using a water molecule as the nucleophile tightly associated to the zinc cofactor. Hammett linear free energy correlations using α-haloacetamido substrate analogues demonstrated the presence of an oxyanion tetrahedral intermediate and significant negative charge development at the transition state. This charge would be stabilized by the oxyanion hole generated by the backbone nitrogen of Tyr145 and the zinc as revealed in the *Cl*CDA crystal structure. It was previously proposed by Hekmat et al. that there are four significant sugar-binding subsites in the active cleft (−2, −1, 0, and +1) that interact with the GlcNAc moieties from the nonreducing to the reducing end of the substrate. The subsites that make the largest contribution to substrate-binding free energy change are −2 and +1 (*31*). Probing of subsite +1 using *p*NPβGlcNAc revealed that the enzyme was still able to slowly de-*N*-acetylate the GlcNAc component, suggesting that the stacking interactions of the phenyl ring with a conserved aromatic amino acid side chain are sufficient to at least partially mimic the reducing end GlcNAc sugar interaction with subsite +1. The presence of the acetamido (*N*-acetyl) group at subsite +1 may not be required, but in the docking studies undertaken this subsite has the only weakly positively charged patch in a predominantly negatively charged catalytic groove, generated primarily by Lys171, which might prevent a de-*N*-acetylated sugar from binding in this subsite. This factor may contribute to the hypothesis that only every second GlcNAc sugar in the substrate is de-*N*-acetylated. This might allow for resistance not only to chitinases, which require the presence of the *N*-acetyl group to facilitate recognition of chitin, but also to chitosanases, which recognize and hydrolyze chitosan, the de-*N*-acetylated form of chitin. It may also present a chitosan-rich matrix with a partial positive charge that might aid interactions with the cell membrane. Hence *Cl*CDA may be an important virulence factor for *C. lindemuthianum*, camouflaging it from host glycosidases as it penetrates and colonizes host tissue. Future studies will be directed toward identification and development of inhibitors of CE-4 esterases to allow the study of their in vivo functions in fungal pathogens.

REFERENCES

1. Bailey, J. A., and Jeger, M. J. (1992) *Colletotrichum: Biology, Pathology and Control*, CAB International, Wallingford.
2. Cano, J., Guarro, J., and Gene, J. (2004) Molecular and morphological identification of *Colletotrichum* species of clinical interest, *J. Clin. Microbiol. 42*, 2450−2454.

3. Broekaert, W. F., Terras, F. R. G., and Cammue, B. P. A. (2000) Induced and preformed antimicrobial proteins, in *Mechanisms of resistance to plant diseases* (Slusarenko, A., Fraser, R. S. S., and Loon, L. C., Eds.) Kluwer Academic, Dordrecht, The Netherlands.
4. Mauch, F., and Staehelin, A. (1989) Functional implications of the subcellular localization of ethylene-induced chitinase and beta-1,3-glucanase in bean leaves, *Plant Cell 1*, 447−457.
5. Boller, T. (1995) Chemoreception of microbial signals in plant cells, *Annu. Rev. Plant Physiol. Plant Mol. Biol. 46*, 189−214.
6. Felix, G., Regenass, M., and Boller, T. (1993) Specific perception of subnanomolar concentrations of chitin fragments by tomato cells: Induction of extracellular alkalinization, changes in protein phosphorylation, and establishment of a refractory state, *Plant J. 4*, 307−316.
7. Vander, P., Varum, K. M., Domard, A., El Gueddari, N. E., and Moerschbacher, B. M. (1998) Comparison of the ability of partially N-acetylated chitosans and chitoologosaccharides to elicit resistance reactions in wheat leaves, *Plant Physiol. 118*, 1353−1359.
8. El Gueddari, N. E., Rauchhaus, U., Moerschbacher, B. M., and Deising, H. B. (2002) Developmentally regulated conversion of surface-exposed chitin to chitosan in cell walls of plant pathogenic fungi, *New Phytol. 156*, 103−112.
9. Ride, J. P., and Barber, M. S. (1990) Purification and characterization of multiple forms of endochitinase from wheat leaves, *Plant Sci. 71*, 185−197.
10. Deising, H., and Siegrist, J. (1995) Chitin deacetylase activity of the rust *Uromyces viciae-fabae* is controlled by fungal morphogenesis, *FEMS Microbiol. Lett. 127*, 207−212.
11. Coutinho, P. M., and Henrissat, B. (1999) Carbohydrate-active enzymes: an integrated database approach, in *Recent advances in carbohydrate bioengineering* (Gilbert, H. J., Davies, G., Henrissat, B., and Svensson, B., Eds.) pp 3−12, The Royal Society of Chemistry, Cambridge, UK.
12. Caufrier, F., Martinou, A., Dupont, C., and Bouriotis, V. (2003) Carbohydrate esterase family 4 enzymes: substrate specificity, *Carbohydr. Res. 338*, 687−692.
13. Long, S. R. (1989) Rhizobium-legume nodulation: life together in the underground, *Cell 56*, 203−214.
14. John, M., Rohrig, H., Schmidt, J., Wieneke, U., and Schell, J. (1993) *Rhizobium* NodB protein involved in nodulation signal synthesis is a chitooligosaccharide deacetylase, *Proc. Natl. Acad. Sci. U.S.A. 90*, 625−629.
15. Fukushima, T., Yamamoto, H., Atrih, A., Foster, S. J., and Sekiguchi, J. (2002) A polysaccharide deacetylase gene (pdaA) is required for germination and for production of muramic delta-lactam residues in the spore cortex of *Bacillus subtilis*, *J. Bacteriol. 184*, 6007−6015.
16. Gilmore, M. E., Bandyopadhyay, D., Dean, A. M., Linnstaedt, S. D., and Popham, D. L. (2004) Production of muramic delta-lactam in *Bacillus subtilis* spore peptidoglycan, *J. Bacteriol. 186*, 80−89.
17. Vollmer, W., and Tomasz, A. (2000) The pgdA gene encodes for a peptidoglycan *N*-acetylglucosamine deacetylase in *Streptococcus pneumoniae*, *J. Biol. Chem. 275*, 20496−20501.
18. Vollmer, W., and Tomasz, A. (2002) Peptidoglycan *N*-acetylglucosamine deacetylase, a putative virulence factor in *Streptococcus pneumoniae*, *Infect. Immun. 70*, 7176−7178.
19. Araki, Y., and Ito, E. (1975) A pathway of chitosan formation in *Mucor rouxii*. Enzymatic deacetylation of chitin, *Eur. J. Biochem. 55*, 71−78.
20. Kafetzopoulos, D., Martinou, A., and Bouriotis, V. (1993) Bioconversion of chitin to chitosan: purification and characterization of chitin deacetylase from *Mucor rouxii*, *Proc. Natl. Acad. Sci. U.S.A. 90*, 2564−2568.
21. Alfonso, C., Nuero, O. M., Santamaria, F., and Reyes, F. (1995) Purification of a heat-stable chitin deacetylase from *Aspergillus nidulans* and its role in cell wall degradation, *Curr. Microbiol. 30*, 49−54.
22. Gao, X. D., Katsumoto, T., and Onodera, K. (1995) Purification and characterization of chitin deacetylase from *Absidia coerulea*, *J. Biochem. (Tokyo) 117*, 257−263.
23. Tsigos, I., and Bouriotis, V. (1995) Purification and characterization of chitin deacetylase from *Colletotrichum lindemuthianum*, *J. Biol. Chem. 270*, 26286−26291.
24. Tokuyasu, K., Ohnishi-Kameyama, M., and Hayashi, K. (1996) Purification and characterization of extracellular chin deacetylase from *Colletotrichum lindemuthianum*, *Biosci., Biotechnol., Biochem. 60*, 1598−1603.
25. Christodoulidou, A., Bouriotis, V., and Thireos, G. (1996) Two sporulation-specific chitin deacetylase-encoding genes are required for the ascospore wall rigidity of *Saccharomyces cerevisiae*, *J. Biol. Chem. 271*, 31420−31425.
26. Christodoulidou, A., Briza, P., Ellinger, A., and Bouriotis, V. (1999) Yeast ascospore wall assembly requires two chitin deacetylase isozymes, *FEBS Lett. 460*, 275−279.
27. Tokuyasu, K., Kaneko, S., Hayashi, K., and Mori, Y. (1999) Production of a recombinant chitin deacetylase in the culture medium of *Escherichia coli* cells, *FEBS Lett. 458*, 23−26.
28. Shrestha, B., Blondeau, K., Stevens, W. F., and Hegarat, F. L. (2004) Expression of chitin deacetylase from *Colletotrichum lindemuthianum* in *Pichia pastoris*: purification and characterization, *Protein Expression Purif. 38*, 196−204.
29. Martinou, A., Koutsioulis, D., and Bouriotis, V. (2002) Expression, purification, and characterization of a cobalt-activated chitin deacetylase (Cda2p) from *Saccharomyces cerevisiae*, *Protein Expression Purif. 24*, 111−116.
30. Tokuyasu, K., Mitsutomi, M., Yamaguchi, I., Hayashi, K., and Mori, Y. (2000) Recognition of chitooligosaccharides and their *N*-acetyl groups by putative subsites of chitin deacetylase from a deuteromycete, *Colletotrichum lindemuthianum*, *Biochemistry 39*, 8837−8843.
31. Hekmat, O., Tokuyasu, K., and Withers, S. G. (2003) Subsite structure of the endo-type chitin deacetylase from a deuteromycete, *Colletotrichum lindemuthianum*: an investigation using steady-state kinetic analysis and MS, *Biochem. J. 374* (Part 2), 369−380.
32. Davies, G. J., Wilson, K. S., and Henrissat, B. (1997) Nomenclature for sugar-binding subsites in glycosyl hydrolases, *Biochem. J. 321* (Part 2), 557−559.
33. Blair, D. E., and van Aalten, D. M. (2004) Structures of *Bacillus subtilis* PdaA, a family 4 carbohydrate esterase, and a complex with *N*-acetyl-glucosamine, *FEBS Lett. 570*, 13−19.
34. Blair, D. E., Schuttelkopf, A. W., Macrae, J. I., and van Aalten, D. M. (2005) Structure and metal-dependent mechanism of peptidoglycan deacetylase, a streptococcal virulence factor, *Proc. Natl. Acad. Sci. U.S.A. 102*, 15429−15434.
35. Taylor, E. J., Gloster, T. M., Turkenburg, J. P., Vincent, F., Brzozowski, A. M., Dupont, C., Shareck, F., Centeno, M. S., Prates, J. A., Puchart, V., Ferreira, L. M., Fontes, C. M., Biely, P., and Davies, G. J. (2006) Structure and activity of two metal-ion dependent acetyl xylan esterases involved in plant cellwall degradation reveals a close similarity to peptidoglycan deacetylases, *J. Biol. Chem. 281*, 10968−10975.
36. Otwinowski, Z., and Minor, W. (1997) Processing of X-ray diffraction data collected in oscillation mode, *Methods Enzymol. 276*, 307−326.
37. Vagin, A., and Teplyakov, A. (1997) MOLREP: an automated program for molecular replacement, *J. Appl. Crystallogr. 30*, 1022−1025.
38. Perrakis, A., Morris, R., and Lamzin, V. S. (1999) Automated protein model building combined with iterative structure refinement, *Nat. Struct. Biol. 6*, 458−463.
39. Brunger, A. T., Adams, P. D., Clore, G. M., DeLano, W. L., Gros, P., Grosse-Kunstleve, R. W., Jiang, J. S., Kuszewski, J., Nilges, M., Pannu, N. S., Read, R. J., Rice, L. M., Simonson, T., and Warren, G. L. (1998) Crystallography & NMR system: A new software suite for macromolecular structure determination, *Acta Crystallogr., Sect. D: Biol. Crystallogr. 54* (Part 5), 905−921.
40. Murshudov, G. N., Vagin, A. A., and Dodson, E. J. (1997) Refinement of macromolecular structures by the maximum-likelihood method, *Acta Crystallogr., Sect. D: Biol. Crystallogr. 53* (Part 3), 240−255.
41. Kleywegt, G. J., and Jones, T. A. (1997) *Model building and refinement practice*, Academic Press, New York.
42. Emsley, P., and Cowtan, K. (2004) Coot: model-building tools for molecular graphics, *Acta Crystallogr., Sect. D: Biol. Crystallogr. 60* (Part 12, Part 1), 2126−2132.
43. Schuttelkopf, A. W., and van Aalten, D. M. (2004) PRODRG: a tool for high-throughput crystallography of protein-ligand complexes, *Acta Crystallogr., Sect. D: Biol. Crystallogr. 60* (Part 8), 1355−1363.

44. DeLano, W. L. (2002) The PyMOL Molecular Graphics System, DeLano Scientific, San Carlos, CA.
45. Morris, G. M., Goodsell, D. S., Halliday, R. S., Huey, R., Hart, W. E., Belew, R. K., and Olson, A. J. (1998) Automated docking using a Lamarckian genetic algorithm and an empirical binding free energy function, *J. Comput. Chem. 19*, 1639−1662.
46. Vriend, G. (1990) WHAT IF: a molecular modeling and drug design program, *J. Mol. Graphics 8*, 52−56, 29.
47. Leatherbarrow, R. J. (2001) GraFit Version 5, Erithacus Software Ltd., Horley, U.K.
48. Fersht, A. (1999) *Structure and mechanism in protein science*, W. H. Freeman, New York.
49. Carroll, F. A. (1998) *Perspectives on structure and mechanism in organic chemistry*, 1st ed., Brooks/Cole Publishing Co., Pacific Grove, CA.
50. Hammett, L. P. (1937) The effect of structure upon the reactions of organic compounds. Benzene derivatives, *J. Am. Chem. Soc 59*, 96−103.
51. Charton, M. (1963) Definition of "inductive" substituent constants, *J. Org. Chem. 29*, 1222−1227.
52. Hansch, C., and Leo, A. (1979) *Substituent constants for correlation analysis in chemistry and biology*, Wiley, New York.
53. Bond, C. S. (2003) TopDraw: a sketchpad for protein structure topology cartoons, *Bioinformatics 19*, 311−31.

BI0606694